SARS-CoV-2 infects lung epithelial cells and induces senescence and an inflammatory response in patients with severe COVID-19

Konstantinos Evangelou[1*], Dimitris Veroutis[1*], Periklis G. Foukas[2*], Koralia Paschalaki[3], Nefeli Lagopati[1], Marios Dimitriou[4], Angelos Papaspyropoulos[1], Orsalia Hazapis[1], Aikaterini Polyzou[1], Sophia Havaki[1], Athanassios Kotsinas[1], Christos Kittas[1], Athanasios G. Tzioufas[5], Laurence de Leval[6], Demetris Vassilakos[1], Sotirios Tsiodras[7,8], Ioannis Karakasiliotis[4], Peter J Barnes[3#] and Vassilis G. Gorgoulis[1,9,10,11#]

1. Molecular Carcinogenesis Group, Department of Histology and Embryology, Medical School, National and Kapodistrian University of Athens, Athens, Greece
2. 2nd Department of Pathology, Attikon University Hospital, Medical School, National and Kapodistrian University of Athens, Athens, Greece
3. Airway Disease Section, National Heart and Lung Institute, Imperial College London, London, UK
4. Laboratory of Biology, Department of Medicine, Democritus University of Thrace, Alexandroupolis, Greece
5. Department of Pathophysiology, Medical School, National and Kapodistrian University of Athens, Athens, Greece
6. Institute of Pathology, Lausanne University Hospital, Lausanne, Switzerland.
7. 4th Department of Internal Medicine, Attikon University Hospital, University of Athens Medical School, Athens, Greece
8. Hellenic Centre for Disease Control and Prevention, Athens, Greece.

9. Faculty Institute for Cancer Sciences, Manchester Academic Health Sciences Centre, University of Manchester, Manchester, UK

10. Biomedical Research Foundation, Academy of Athens, Athens, Greece

11. Center for New Biotechnologies and Precision Medicine, Medical School, National and Kapodistrian University of Athens, Athens, Greece

***equally contributed**

Key words: SARS-Cov-2, monoclonal antibody, COVID-19, cellular senescence, senescence-associated secretory phenotype (SASP), angiotensin-converting-enzyme 2 (ACE2), alveolar type-2 (AT2) cells, DNA damage, SenTraGor

Short title: SARS-Cov-2 infected human alveolar cells exhibit features of cellular senescence

 # Corresponding Authors: Peter J Barnes, p.j.barnes@imperial.ac.uk

Vassilis G Gorgoulis, vgorg@med.uoa.gr

Abstract

Rationale: SARS-CoV-2 infection of the respiratory system can progress to a life threatening multi-systemic disease, mediated via an excess of cytokines ("cytokine storm"), but the molecular mechanisms are poorly understood.

Objectives: To investigate whether SARS-CoV-2 may induce cellular senescence in lung epithelial cells, leading to secretion of inflammatory cytokines, known as the senescence-associated secretory phenotype (SASP).

Methods: Autopsy lung tissue samples from eleven COVID-19 patients and sixty age-matched non-infected controls were analysed by immunohistochemistry for SARS-CoV-2 and markers of cellular senescence (SenTraGor, $p16^{INK4A}$) and key SASP cytokines (interleukin-1β, interleukin-6). We also investigated whether SARS-CoV-2 infection of an epithelial cell line induces senescence and cytokine secretion.

Measurements and Main Results: SARS-CoV-2 was detected by immunocytochemistry and electron microscopy predominantly in alveolar type-2 (AT2) cells, which also expressed the angiotensin-converting-enzyme 2 (ACE2), a critical entry receptor for this virus. In COVID-19 samples, AT2 cells displayed increased markers of senescence [$p16^{INK4A}$, SenTraGor staining positivity in 12±1.2% of cells compared to 1.7±0.13% in non-infected controls ($p<0.001$)], with markedly increased expression of interleukin-1β and interleukin-6 ($p<0.001$). Infection of epithelial cells (Vero E6) with SARS-CoV-2 *in-vitro* induced senescence and DNA damage (increased SenTraGor and γ-H2AX), and reduced proliferation (Ki67) compared to uninfected control cells ($p<0.01$).

64 **Conclusions:** We demonstrate that in severe COVID-19 patients, AT2 cells are infected
65 with SARS-CoV-2 and show senescence and expression of proinflammatory cytokines. We
66 also show that SARS-CoV-2 infection of epithelial cells may induce senescence and
67 inflammation, indicating that cellular senescence may be an important molecular
68 mechanism of severe COVID-19.
69
70

Introduction

The severe acute respiratory syndrome coronavirus 2 (SARS-CoV-2) causes the Coronavirus disease 2019 (COVID-19) that primarily affects the respiratory system. The clinical course of the patients ranges from asymptomatic to a life-threatening respiratory failure accompanied by a multi-systemic inflammatory disease (1,2). Systemic disease may occur through a viral-mediated "cytokine storm" that consists of a variety of cytokines and chemokines (CXCL-10, CCL-2, IL-6, IL-8, IL-12, IL1β, IFN-γ, TNF-α) (3,4). The link between viral infection of cells and development of severe lung disease and systemic manifestations is still poorly understood. Viral infection results in the activation of complex innate and adaptive immune responses that are orchestrated sequentially, involving several cell types and inflammatory mediators (5,6). At the cellular level, intrinsic defence mechanisms are activated and outcomes range from complete recovery to cell death (7-11). An “intermediate” and essential cellular state that is overlooked, due to lack of efficient methodological tools, is cellular senescence (12,13).

Cellular senescence is a stress response mechanism that preserves organismal homeostasis. Senescent cells are characterized by prolonged and generally irreversible cell-cycle arrest and resistance to apoptosis (12,14). Additionally, they also exhibit secretory features collectively described, as the senescence-associated secretory phenotype (SASP) (12). SASP includes a variety of cytokines, chemokines, growth factors, proteases and other molecules, depending on the senescence type (12,15). They are released in the extracellular space as soluble factors, transmembrane proteins following ectodomain shedding, or as molecules engulfed within small exosome-like vesicles (16-18). Under physiological conditions, senescence is transiently activated and SASP

mediates the recruitment of immune cells for senescent cell clearance. In addition, other SASP factors promote tissue regeneration and repair, overall ensuring cellular/tissue homeostasis. On the contrary, persistence of senescent cells exerts harmful properties promoting tissue dysfunction and the maintenance of a "latent" chronic inflammatory milieu, via paracrine and systemic SASP (12,15).

There is little published evidence linking viral infection to cellular senescence (19-22). Given the significance of the "cytokine storm" in the progression of COVID-19 and the SASP secretion by senescent cells, we investigated whether cellular senescence occurs in COVID-19. We provide the first evidence supporting not only the evidence for senescence in COVID-19 infected lung cells, but also potential long-term adverse implications of this disease process.

Materials and Methods

Lung tissue

Formalin Fixed and Paraffin embedded autopsy lung tissue samples from eleven patients that died from COVID-19 (confirmed by RT-qPCR) and lung tissues resected prior to the COVID-19 outbreak, comprising a cohort of sixty previously published and new cases (negative controls) were analyzed (**Suppl. Table 1**) (23). Clinical sample collection and their experimental use were approved by the Commission Cantonale D'éthique de la Recherche, University of Lausanne, Switzerland (Ref 2020-01257), the Bio-Ethics Committee of University of Athens Medical School, Greece.

Anti-SARS-COV-2 (G2) antibody generation

Mice immunization and antibodies collection, selection and specificity determination are described in detail in **Suppl Information**. Transcriptome analysis of hybridomas and amino acid determination of selected clones are also provided in **Suppl Information**. Four clones, namely 479-S1, 480-S2, 481-S3 and 482-S4 are under patent application **(Gorgoulis V.G., Vassilakos D. and Kastrinakis N. (2020) GR-patent application no: 22-0003846810).**

Cells and SARS-CoV-2 culture

SARS-CoV-2 [isolate 30-287 (B.1.222 strain)] was obtained through culture in Vero E6 cells (ATCC® CRL-1586), from an infected patient in Greece. The virus was recovered from a nasopharyngeal swab, rinsed in 1 ml saline and filtered twice through a 0.22 nm filter.

129 Virus stock was prepared by infecting fully confluent Vero E6 cells in DMEM, 10% fetal
130 bovine serum (FBS), with antibiotics, at 37°C, 5% CO_2. Virus stock was collected four days
131 after inoculation, sequenced by NGS (**Suppl Information**) and the supernatant was frozen
132 (−80°C) until use. Infections were carried out in 24-well plates, using SARS-CoV-2 at a 0.01
133 MOI. Cells were either fixed with 4% paraformaldehyde or lysed with NucleoZOL
134 (MACHEREY-NAGEL) 17 days post infection. Manipulations were carried out in a Biosafety
135 level 3 facility.
136
137 **RNA extraction and Reverse-Transcription real-time PCR (RT-qPCR)** detection were
138 performed as previously described (**Suppl Information**) (24).
139
140 **Next Generation Sequencing (NGS)**
141 NGS was performed as previously described (25). Briefly, the Ion AmpliSeq Library Kit
142 Plus was used to generate libraries following the manufacturer's instruction, employing
143 the Ion AmpliSeq SARS-CoV-2 RNA custom primers panel (ID: 05280253, Thermo Fisher
144 Scientific). Briefly, library preparation steps involved reverse transcription of RNA using
145 the SuperScript VILO cDNA synthesis kit (Thermo Fisher Scientific), 17-19 cycles of PCR
146 amplification, adapter ligation, library purification using the Agencourt_AMPure XP
147 (Beckman Coulter), and library quantification using Qubit Fluorometer high-sensitivity kit.
148 Ion 530 Chips were prepared using Ion Chef and NGS reactions were run on an Ion
149 GeneStudio S5, ion torrent sequencer (Thermo Fisher Scientific). Samples were run in
150 triplicates.
151

152 **Immunocytochemistry and Immunohistochemistry**

153 ICC and IHC were performed according to published protocols (26). The following primary
154 antibodies were applied overnight at 4°C: i) anti-SARS-CoV-2 (G2) monoclonal antibody
155 (at a dilution 1:300), ii) anti-ACE-2 (Abcam), iii) anti- TTF-1 (Dako), iv) anti-CD68 (Dako)
156 and v) anti-p16^{INK4A} (Santa Cruz), vi) anti-IL-1β (Abcam) and vii) anti-IL-6 (R&D systems),
157 viii) anti- phospho-histone (Ser 139) 2AX (γH2AX) (Cell Signaling) and ix) anti-Ki67
158 (Abcam)(**Suppl Information**).

159

160 **SenTraGor™ staining and double staining** experiments were performed and evaluated
161 as previously described (26).

162

163 **Electron Microscopy**

164 Representative area from hematoxylin and eosin stained paraffin sections of the lung
165 autopsy of COVID-19 patients and corresponding non COVID-19 controls were chosen
166 under the light microscope and marked. Paraffin-embedded tissue was deparaffinized,
167 rehydrated and fixed in 2.5% glutaraldehyde in PBS for 24h and post-fixed in 1% aqueous
168 osmium tetroxide for 1h at 4°C. The tissue fragment was embedded in fresh epoxy resin
169 mixture, stained with ethanolic uranyl acetate and lead citrate and observed with a FEI
170 Morgagni 268 transmission electron microscope equipped with Olympus Morada digital
171 camera.

172

173 **Statistical analysis**

174 The Wilcoxon paired non-parametric test was used to compare GL13 labelling indices and

175 levels of IL-6, IL-8 and IL-1β between two groups (non-COVID-19 and COVID-19 infected).

176

Results

Detection of SARS-CoV-2 in lung cells

In order to detect SARS-CoV2 in lung tissue we developed monoclonal antibodies which react against the spike protein of SARS-CoV-2 and identified a high affinity antibody (G2) (**Suppl Figure 1, Suppl Figure 2, Suppl. Table 1A and Suppl. Table 1B)** (23). SARS-CoV-2 was detected predominantly in alveolar type 2 (AT2) cells, which are identified by TTF-1 positivity, and in sparse inflammatory cells (alveolar and tissue macrophages) in all COVID-19 patients (**Figure 1A, C**), ranging from <5 cells/4mm^2 tissue to >50 cells/4mm^2 tissue (**Suppl. Table 1A**). SARS-CoV-2 infected AT2 cells were occasionally large and appeared isolated (denuded or syncytial) or clustered (hyperplasia), exhibiting a variety of topological distribution (**Figure 1A**). These cells co-expressed the angiotensin-converting enzyme 2 (ACE2) receptor (**Figure 1B**), supporting SARS-Cov-2 infection being mediated by the ACE2 receptor (27). In addition, electron microscopy analysis in representative COVID-19 cases confirmed the presence of virus within AT2 cells (**Figure 1Ci,ii**) and high magnification revealed virions in the proximity of the endoplasmic reticulum (**Figure 1Ciii,iv**) indicating their likely assembly and budding, as well as virions residing in cytoplasmic vesicles (**Figure 1Ciii,v-vi**), implying their transfer and release into the extracellular space.

Senescence in SARS-CoV-2 infected cells

A proportion of SARS-CoV-2 infected AT2 cells (range 8 to 21%) displayed a senescent phenotype, with positive staining for SenTraGor and p16^{INK4A} (**Figure 2A-C**) (12,26-28). By

contrast lung tissues from age-matched non-COVID-19 cases with analogous co-morbidities (**Suppl Table 1**) showed significantly lower senescence (range 1-2%, $p<0.01$, Wilcoxon paired non-parametric test) (**Figure 2A-C**), suggesting that SARS-CoV-2 infection may induce senescence.

To functionally reproduce our hypothesis we infected Vero cells with a viral strain isolated from a COVID-19 patient. Vero cells is an established cellular system for viral propagation and studies, as apart from their high infectivity to SARS-CoV-2 they are among the few cell lines demonstrating SARS-CoV-2-mediated cytopathic effects, an essential aspect in diagnostics (29,30). Infection was carried out at a low MOI to mimic natural coronavirus infection (31). In line with our hypothesis, the infected cells following an initial surge of cell death reached an equilibrium demonstrating clear evidence of senescence, as compared to the non-infected control cells, 17 days post infection (**Figure 3**). As Vero cells lack $p16^{INK4A}$ (32), the most likely trigger of senescence is DNA damage, as previously reported (12,33). DNA damage measured by γ-H2AX immunostaining, was evident in SARS-CoV-2 infected cells (**Figure 3A4**). It appears that genotoxic stress results from a vicious cycle imposed by the virus in host cells as it high-jacks most intracellular protein machineries (11,34).

Senescence associated secretory phenotype

We found very high expression of both IL-1β and IL-6 by senescent AT2 cells in the lungs of COVID-19 patients while in the non COVID-19 control cases expression was very low in the few senescent AT2 cells detected ($p<0.001$) (**Figure 4A-C, Suppl Table 1**). As both cytokines are key components of the "cytokine storm", our findings suggest putative

223 implication of senescence via SASP in the poor clinical course of COVID-19 patients.
224 Likewise, SARS-CoV-2 senescent Vero cells displayed expression of SASP-related
225 cytokines, as assessed by our recently reported algorithmic assessment of senescence,
226 justifying the *in vivo* findings (**Figure 3B**).
227
228

Discussion

We have demonstrated the presence of SARS-CoV-2 in AT2 cells of patients who died from COVID-19 using a novel anti-viral antibody and confirmed by electron microscopy. We have shown for the first time that a proportion of SARS-CoV-2-infected AT2 cells acquire senescence features (as demonstrated by significantly increased staining with the novel senescence marker SenTraGor and increased $p16^{INK4A}$). The finding that in age-matched non-COVID-19 cases the percentage of senescent cells was much lower (1-2%) than that of the COVID-19 clinical panel (8-21%), is strongly indicative that SARS-CoV-2 triggers senescence (**Figure 2**). We therefore examined whether cellular infection with SARS-CoV-2 virus (B.1.222 strain) would induce cellular senescence in a susceptible cell line *in vitro* and found that in infected cells there was increased SenTraGor staining, as well as evidence of DNA damage measured by increased γ-H2AX expression. This strongly suggests that SARS-CoV-2 may attach to AT2 cells via ACE2 to infect these cells and through activation of the DNA damage response may induce cellular senescence (34). We also demonstrated that the cells infected with SARS-CoV-2 also show a high degree of expression of IL-1β and IL-6, both components of the SASP and implicated in systemic features of COVID-19 which is associated with a "cytokine storm" (3,4).

Senescent cells are in a state of cell cycle arrest but remain metabolically active and secrete a typical profile of inflammatory proteins known as the senescence-associated secretory phenotype (SASP). SASP components include the proinflammatory cytokines IL-1β and Il-6, which are elevated in COVID-19 patients that have acute respiratory distress syndrome (ARDS) or systemic inflammatory features. The SASP components could induce senescence in nearby cells (paracrine) or may spread senescence systemically

(endocrine), thus amplifying this chronic inflammation. It is likely that SARS-CoV-2 spreads from epithelial cells in the lower airways to infect AT2 cells, which express ACE2, and cause local senescence and inflammation in the lung. The virus may then enter the circulation and senescence may subsequently spread systemically to affect other organs, leading to multi-organ failure and death (1,22)

An additional implication relates to the prolonged survival of senescent cells that are infected with the virus, as senescent cells are resistant to apoptosis (12,14). This may allow the virus to be hosted for longer periods compared to other cells with higher cell turnover, exposing its genome to host-mediated editing (35-38). Within this context, we recently reported abundance of the APOBEC enzymes, particularly G and H (RNA editing cytoplasmic variants), which are reported to play a pivotal role in viral RNA editing, in cells undergoing stress-induced senescence (24,39,40). In support to this notion, are the increased APOBEC 3G and 3H expression levels found in the infected Vero cells (**Suppl Figure 3)**. Moreover, by conducting a detailed bioinformatic analysis of 423000 SARS-CoV-2 strains available in the GISAID database, we found that APOBEC signatures seem to potently determine the mutational profile of the SARS-CoV-2 genome (**Suppl Figure 4, Suppl Figure 5).**

A limitation of the study is the small sample size of examined COVID-19 lung autopsies, due to difficulty of getting access to this material. Another limitation due to the nature of the disease is that pathological features, such as senescence, can only be investigated within the context of cadaverous material, which represents the most severe outcome of the spectrum of COVID-19 clinical manifestations. Therefore, evaluation of senescence in

less severe conditions is not feasible. Findings have been observed in lung biopsies only and ideally should be also investigated in organs other than the lung.

Overall, SARS-CoV-2 induced senescence justifies the application of senotherapeutics not only as a therapeutic approach for the treatment of COVID-19 patients but also as a putative strategy to restrict mutational events that may favor the emergence of SARS-CoV-2 quasispecies (15,22,41). Senotherapies include senostatics that inhibit components of the cellular senescence pathways and senolytics, which induce senescent cells to become apoptotic (15,22). Several senolytic therapies have been shown to be effective in animal models of accelerated ageing diseases, including COPD, idiopathic pulmonary fibrosis, atherosclerosis and chronic kidney disease (12,15,22). A trial of senolytic therapy in patients with diabetic kidney disease demonstrated a reduction in senescent cells in the skin and reduced circulating SASP proteins, such as IL-1β and IL-6 (42). A clinical trial of a Senolytic compound (F) to inhibit progression to cytokine storm and ARDS in COVID-19 patients has been approved by the US Food and Drug Administration (FDA) and is anticipated to be soon launched (43).

Disclosure/Conflict of Interest

The authors wish to declare no conflict of interest.

Acknowledgements:

We would like to thank Konstantinos Ntostoglou for his valuable help in preparing the material. We acknowledge support in RNA sequencing by the "The Greek Research

297 Infrastructure for Personalised Medicine (pMED-GR)" (MIS 5002802) which is
298 implemented under the Action "Reinforcement of the Research and Innovation
299 Infrastructure", funded by the Operational Programme "Competitiveness,
300 Entrepreneurship and Innovation" (NSRF 2014-2020) and co-financed by Greece and the
301 European Union (European Regional Development Fund). This work was supported by
302 the: National Public Investment Program of the Ministry of Development and Investment
303 / General Secretariat for Research and Technology, in the framework of the Flagship
304 Initiative to address SARS-CoV-2 (2020ΣΕ01300001); Horizon 2020 Marie Sklodowska-
305 Curie training program no. 722729 (SYNTRAIN); Welfare Foundation for Social & Cultural
306 Sciences, Athens, Greece (KIKPE); H. Pappas donation; Hellenic Foundation for Research
307 and Innovation (HFRI) grants no. 775 and 3782 and NKUA-SARG grant 70/3/8916.

308

309

References

1. Hu B, Guo H, Zhou P, Shi ZL. Characteristics of SARS-CoV-2 and COVID-19. Nat Rev Microbiol 2021; 19: 141–154.

2. Robba C, Battaglini D, Ball L, Patroniti N, Loconte M, Brunetti I, Vena A, Giacobbe DR, Bassetti M, Rocco PRM, Pelosi P. Distinct phenotypes require distinct respiratory management strategies in severe COVID-19. Respir Physiol Neurobiol 2020; 279: 103455.

3. Del Valle DM, Kim-Schulze S, Huang HH, Beckmann ND, Nirenberg S, Wang B, Lavin Y, Swartz TH, Madduri D, Stock A, Marron TU, Xie H, Patel M, Tuballes K, Van Oekelen O, Rahman A, Kovatch P, Aberg JA, Schadt E, Jagannath S, Mazumdar M, Charney AW, Firpo-Betancourt A, Mendu DR, Jhang J, Reich D, Sigel K, Cordon-Cardo C, Feldmann M, Parekh S, Merad M, Gnjatic S. An inflammatory cytokine signature predicts COVID-19 severity and survival. Nat Med 2020: 26: 1636–1643.

4. Tang Y, Liu J, Zhang D, Xu Z, Ji J, Wen C. Cytokine Storm in COVID-19: The Current Evidence and Treatment Strategies. Front Immunol 2020; 11: 1708.

5. Poland GA, Ovsyannikova IG, Kennedy RB. SARS-CoV-2 immunity: review and applications to phase 3 vaccine candidates. Lancet 2020; 396: 1595–1606.

6. Zhang F, Gan R, Zhen Z, Hu X, Li X, Zhou F, Liu Y, Chen C, Xie S, Zhang B, Wu X, Huang Z. Adaptive immune responses to SARS-CoV-2 infection in severe versus mild individuals. Signal Transduct Target Ther 2020; 5: 156.

7. Rouse BT, Sehrawat S. Immunity and immunopathology to viruses: what decides the outcome? Nat Rev Immunol 2010; 10: 514–526.

8. Mocarski ES, Upton JW, Kaiser WJ. Viral infection and the evolution of caspase 8-regulated apoptotic and necrotic death pathways. Nat Rev Immunol 2011; 12: 79–88.

9. Braciale TJ, Sun J, Kim TS. Regulating the adaptive immune response to respiratory virus infection. Nat Rev Immunol 2012; 12: 295–305.

10. Fan Y, Sanyal S, Bruzzone R. Breaking Bad: How Viruses Subvert the Cell Cycle. Front Cell Infect Microbiol 2018; 8: 396.

11. Hekman RM, Hume AJ, Goel RK, Abo KM, Huang J, Blum BC, Werder RB, Suder EL, Paul I, Phanse S, Youssef A, Alysandratos KD, Padhorny D, Ojha S, Mora-Martin A, Kretov D, Ash PEA, Verma M, Zhao J, Patten JJ, Villacorta-Martin C, Bolzan D, Perea-Resa C, Bullitt E, Hinds A, Tilston-Lunel A, Varelas X, Farhangmehr S, Braunschweig U, Kwan JH, McComb M, Basu A, Saeed M, Perissi V, Burks EJ, Layne MD, Connor JH, Davey R, Cheng JX, Wolozin BL, Blencowe BJ, Wuchty S, Lyons SM, Kozakov D, Cifuentes D, Blower M, Kotton DN, Wilson AA, Mühlberger E, Emili A. Actionable Cytopathogenic Host Responses of Human Alveolar Type 2 Cells to SARS-CoV-2. Mol Cell 2021; 81: 212.

12. Gorgoulis V, Adams PD, Alimonti A, Bennett DC, Bischof O, Bishop C, Campisi J, Collado M, Evangelou K, Ferbeyre G, Gil J, Hara E, Krizhanovsky V, Jurk D, Maier AB, Narita M, Niedernhofer L, Passos JF, Robbins PD, Schmitt CA, Sedivy J, Vougas K, von Zglinicki T, Zhou D, Serrano M, Demaria M. Cellular Senescence: Defining a Path Forward. Cell 2019; 179: 813–827.

13. Rendeiro AF, Ravichandran H, Bram Y, Salvatore S, Borczuk A, Elemento O, Schwartz RE. The spatio-temporal landscape of lung pathology in SARS-CoV-2 infection. medRxiv: the preprint server for health sciences, 2020.10.26.20219584.

14. Childs BG, Baker DJ, Kirkland JL, Campisi J, van Deursen JM. Senescence and apoptosis: dueling or complementary cell fates? EMBO Rep 2014; 15: 1139–1153.

355 15. Myrianthopoulos V, Evangelou K, Vasileiou PVS, Cooks T, Vassilakopoulos TP,
356 Pangalis GA, Kouloukoussa M, Kittas C, Georgakilas AG, Gorgoulis VG. Senescence and
357 senotherapeutics: a new field in cancer therapy. Pharmacol Ther 2019; 193: 31–49.
358 16. Özcan S, Alessio N, Acar MB, Mert E, Omerli F, Peluso G, Galderisi U. Unbiased
359 analysis of senescence associated secretory phenotype (SASP) to identify common
360 components following different genotoxic stresses. Aging 2016; 8: 1316–1329.
361 17. Basisty N, Kale A, Jeon OH, Kuehnemann C, Payne T, Rao C, Holtz A, Shah S, Sharma
362 V, Ferrucci L, Campisi J, Schilling B. A proteomic atlas of senescence-associated
363 secretomes for aging biomarker development. PLoS Biol 2020; 18: e3000599.
364 18. Faget DV, Ren Q, Stewart SA. Unmasking senescence: context-dependent effects of
365 SASP in cancer. Nat Rev Cancer 2019; 19: 439–453.
366 19. Baz-Martínez M, Da Silva-Álvarez S, Rodríguez E, Guerra J, El Motiam A, Vidal A,
367 García-Caballero T, González-Barcia M, Sánchez L, Muñoz-Fontela C, Collado M, Rivas C.
368 Cell senescence is an antiviral defense mechanism. Sci Rep 2016; 6: 37007.
369 20. Chuprin A, Gal H, Biron-Shental T, Biran A, Amiel A, Rozenblatt S, Krizhanovsky V.
370 Cell fusion induced by ERVWE1 or measles virus causes cellular senescence. Genes Dev
371 2013; 27: 2356–2366.
372 21. Kelley WJ, Zemans RL, Goldstein DR. Cellular senescence: friend or foe to
373 respiratory viral infections? Eur Respir J 2020; 56: 2002708.
374 22. Kohli J, Veenstra I, Demaria M. The struggle of a good friend getting old: cellular
375 senescence in viral responses and therapy. EMBO Rep 2021; 22: e52243.
376 23. Gorgoulis VG, Vassiliou LV, Karakaidos P, Zacharatos P, Kotsinas A, Liloglou T,
377 Venere M, Ditullio RA Jr, Kastrinakis NG, Levy B, Kletsas D, Yoneta A, Herlyn M, Kittas C,

Halazonetis TD. Activation of the DNA damage checkpoint and genomic instability in human precancerous lesions. Nature 2005; 434: 907–913.

24. Komseli ES, Pateras IS, Krejsgaard T, Stawiski K, Rizou SV, Polyzos A, Roumelioti FM, Chiourea M, Mourkioti I, Paparouna E, Zampetidis CP, Gumeni S, Trougakos IP, Pefani DE, O'Neill E, Gagos S, Eliopoulos AG, Fendler W, Chowdhury D, Bartek J, Gorgoulis VG. A prototypical non-malignant epithelial model to study genome dynamics and concurrently monitor micro-RNAs and proteins in situ during oncogene-induced senescence. BMC Genomics 2018; 19: 37.

25. Lagopati N, Tsioli P, Mourkioti I, Polyzou A, Papaspyropoulos A, Zafiropoulos A, Evangelou K, Sourvinos G, Gorgoulis VG. Sample pooling strategies for SARS-CoV-2 detection. J Virol Methods 2021; 289: 114044.

26. Evangelou K, Lougiakis N, Rizou SV, Kotsinas A, Kletsas D, Muñoz-Espín D, Kastrinakis NG, Pouli N, Marakos P, Townsend P, Serrano M, Bartek J, Gorgoulis VG. Robust, universal biomarker assay to detect senescent cells in biological specimens. Aging Cell 2017; 16: 192–197.

27. Wang Q, Zhang Y, Wu L, Niu S, Song C, Zhang Z, Lu G, Qiao C, Hu Y, Yuen KY, Wang Q, Zhou H, Yan J, Qi J. Structural and Functional Basis of SARS-CoV-2 Entry by Using Human ACE2. Cell 2020; 181: 894–904.e9.

28. Kohli J, Wang B, Brandenburg SM, Basisty N, Evangelou K, Varela-Eirin M, Campisi J, Schilling B, Gorgoulis V, Demaria M. Algorithmic assessment of cellular senescence in experimental and clinical specimens. Nat Protoc 2021; 10.1038/s41596-021-00505-5. Advance online publication.

400 29. Wurtz N, Penant G, Jardot P, Duclos N, La Scola B. Culture of SARS-CoV-2 in a panel
401 of laboratory cell lines, permissivity, and differences in growth profile. Eur J Clin Microbiol
402 Infect Dis. 2021; 40: 477–484.
403 30. Chu H, Chan JF, Yuen TT, Shuai H, Yuan S, Wang Y, Hu B, Yip CC, Tsang JO, Huang X,
404 Chai Y, Yang D, Hou Y, Chik KK, Zhang X, Fung AY, Tsoi HW, Cai JP, Chan WM, Ip JD, Chu
405 AW, Zhou J, Lung DC, Kok KH, To KK, Tsang OT, Chan KH, Yuen KY. Comparative tropism,
406 replication kinetics, and cell damage profiling of SARS-CoV-2 and SARS-CoV with
407 implications for clinical manifestations, transmissibility, and laboratory studies of COVID-
408 19: an observational study. Lancet Microbe 2020; 1(1): e14–e23.
409 31. Matsuyama S, Ujike M, Morikawa S, Tashiro M, Taguchi F. Protease-mediated
410 enhancement of severe acute respiratory syndrome coronavirus infection. Proc Natl Acad
411 Sci U S A 2005; 102: 12543–12547.
412 32. Osada N, Kohara A, Yamaji T, Hirayama N, Kasai F, Sekizuka T, Kuroda M, Hanada K.
413 The genome landscape of the african green monkey kidney-derived vero cell line. DNA
414 Res 2014; 21: 673–683.
415 33. Bartkova J, Rezaei N, Liontos M, Karakaidos P, Kletsas D, Issaeva N, Vassiliou LV,
416 Kolettas E, Niforou K, Zoumpourlis VC, Takaoka M, Nakagawa H, Tort F, Fugger K,
417 Johansson F, Sehested M, Andersen CL, Dyrskjot L, Ørntoft T, Lukas J, Kittas C, Helleday T,
418 Halazonetis TD, Bartek J, Gorgoulis VG. Oncogene-induced senescence is part of the
419 tumorigenesis barrier imposed by DNA damage checkpoints. Nature 2006; 444: 633–637.
420 34. Gorgoulis VG, Pefani DE, Pateras IS, Trougakos IP. Integrating the DNA damage and
421 protein stress responses during cancer development and treatment. J Pathol 2018: 246:
422 12-40.

423 35. Herranz N, Gil J. Mechanisms and functions of cellular senescence. J Clin Invest
424 2018; 128: 1238–1246.
425 36. Zamaraev AV, Zhivotovsky B, Kopeina GS. Viral Infections: Negative Regulators of
426 Apoptosis and Oncogenic Factors. Biochemistry (Mosc) 2020; 85: 1191–1201.
427 37. Li S, Zhang Y, Guan Z, Li H, Ye M, Chen X, Shen J, Zhou Y, Shi ZL, Zhou P, Peng K.
428 SARS-CoV-2 triggers inflammatory responses and cell death through caspase-8 activation.
429 Signal Transduct Target Ther 2020; 5: 235.
430 38. Ren Y, Shu T, Wu D, Mu J, Wang C, Huang M, Han Y, Zhang XY, Zhou W, Qiu Y, Zhou
431 X. The ORF3a protein of SARS-CoV-2 induces apoptosis in cells. Cell Mol Immunol 2020;
432 17: 881–883.
433 39. Venkatesan S, Angelova M, Puttick C, Zhai H, Caswell DR, Lu WT, Dietzen M,
434 Galanos P, Evangelou K, Bellelli R, Lim EL, Watkins TBK, Rowan A, Teixeira VH, Zhao Y,
435 Chen H, Ngo B, Zalmas LP, Al Bakir M, Hobor S, Gronroos E, Pennycuick A, Nigro E,
436 Campbell BB, Brown WL, Akarca AU, Marafioti T, Wu MY, Howell M, Boulton SJ, Bertoli C,
437 Fenton TR, de Bruin RAM, Maya-Mendoza A, Santoni-Rugiu E, Hynds RE, Gorgoulis VG,
438 Jamal-Hanjani M, McGranahan N, Harris RS, Janes SM, Bartkova J, Bakhoum SF, Bartek J,
439 Kanu N, Swanton C, Consortium T. Induction of APOBEC3 exacerbates DNA replication
440 stress and chromosomal instability in early breast and lung cancer evolution. Cancer
441 Discov 2021; candisc.0725.2020.
442 40. Chemudupati M, Kenney AD, Bonifati S, Zani A, McMichael TM, Wu L, Yount JS.
443 From APOBEC to ZAP: Diverse mechanisms used by cellular restriction factors to inhibit
444 virus infections. Biochim Biophys Acta Mol Cell Res. 2019; 1866: 382-394.

445 41. Malavolta M, Giacconi R, Brunetti D, Provinciali M, Maggi F. Exploring the Relevance
446 of Senotherapeutics for the Current SARS-CoV-2 Emergency and Similar Future Global
447 Health Threats. Cells 2020; 9: 909.
448 42. Hickson LJ, Langhi Prata LGP, Bobart SA, Evans TK, Giorgadze N, Hashmi SK, Herrmann
449 SM, Jensen MD, Jia Q, Jordan KL, Kellogg TA, Khosla S, Koerber DM, Lagnado AB, Lawson
450 DK, LeBrasseur NK, Lerman LO, McDonald KM, McKenzie TJ, Passos JF, Pignolo RJ,
451 Pirtskhalava T, Saadiq IM, Schaefer KK, Textor SC, Victorelli SG, Volkman TL, Xue A,
452 Wentworth MA, Wissler Gerdes EO, Zhu Y, Tchkonia T, Kirkland JL. Senolytics decrease
453 senescent cells in humans: Preliminary report from a clinical trial of Dasatinib plus
454 Quercetin in individuals with diabetic kidney disease. EBioMedicine 2019; 47: 446-456.
455 43. Kirkland JL, Tchkonia T. Senolytic drugs: from discovery to translation. J Intern Med
456 2020; 288: 518–536.
457

458 **Figure Legends**

459

460 **Figure 1: Detection of SARS-CoV-2 in lung cells. A.** Representative images of SARS-CoV-2
461 IHC staining in COVID-19 lung tissue. Competition with anti-peptide (S protein) showing
462 specificity of the IHC staining. Representative negative, control IHC staining in non-
463 COVID-19 lung tissues. Graph shows quantification of SARS-CoV-2 staining in the clinical
464 samples (**Suppl Table 1**). **B.** Detection of SARS-CoV-2 in AT2 cells (confirmed by TTF-1
465 staining) and in ACE-2 expressing cells. Double IHC staining for SARS-CoV-2 and TTF-1. **C.**
466 Detection of SARS-CoV-2 by transmission electron microscopy (TEM) in a representative
467 COVID-19 patient. Presence of SARS-CoV-2 within AT2 cells (**i,ii**) and of virions in the
468 proximity of the endoplasmic reticulum (**iii,iv**) as well as in cytoplasmic vesicles (**iii,v-vi**).
469 Corresponding scale bars are depicted. ICH: immunohistochemistry; AT2: alveolar type 2
470 cells; ACE2: angiotensin-converting enzyme 2, ***Statistical significant: $p<0.001$.

471

472 **Figure 2: Senescence in SARS-CoV-2 infected cells. A.** Representative images of SARS-
473 CoV-2, SenTraGor (senescence) and ACE-2 staining in serial sections of COVID-19 lung
474 tissue**.** Double-immunostaining analysis (**2**) for SARS-CoV-2, SenTraGor (senescence),
475 ACE-2 and $p16^{INK4A}$ in COVID-19 lung tissue**. B.** Representative results from serial staining
476 for SARS-CoV-2, SenTraGor (senescence) and ACE-2, and double-staining experiment for
477 SARS-CoV-2 and $p16^{INK4A}$ in non-COVID-19 lung tissue**. C.** Graphs depicting the increased
478 levels of SenTraGor and $p16^{INK4A}$ in COVID-19 lung tissue**.** Corresponding scale bars are
479 depicted. Statistical significance: **: $p<0.01$; ***: $p<0.001$.

480

Figure 3. SARS-CoV-2 infection, senescence and SASP expression in Vero cells. A. SARS-CoV-2 presence (**1**), senescence induction (**2**), cellular proliferation (**3**) and DNA damage activation (**4**), with corresponding quantitative histograms, in Vero cells with and without SARS-CoV-2 infection. Double IHC staining for SARS-CoV-2 infection/senescence induction (**5**) and senescence induction/cellular proliferation (**6**). **B.** Graph depicting induction of SASP related cytokines following SARS-CoV-2 infection (mRNA expression). **Statistical significant: $p<0.01$.

Figure 4: Senescence associated secretory phenotype (SASP) in COVID-19 lung tissues. A. Representative staining results (at low and high magnification) of SenTraGor, IL-6, IL-1β and TTF-1 in corresponding serial sections (**1**) and as double immunostaining analysis (**2**) of COVID-19 lung tissue. Original magnification: 400x**. B.** Representative staining results showing absence or minimal levels of SenTraGor, IL-6 and IL-1β in age-matched non-COVID-19 ocntrol samples. Corresponding scale bars are depicted. IL-1 β: Interleukin 1β; IL-6: Interleukin-6; ***Statistical significant: $p<0.0001$.

Supplementary Information

Suppl Figure legends

Suppl Figure 1: SARS-CoV-2 antibody production and screening selection. A. Workflow of the procedure for antibody production. **B.** Sequel of screening steps for antibody production and selection. **C.** Final screening step processes leading to the selection of G2 monoclonal antibody (**Suppl Figure 2**).

Suppl Figure 2: Graph depicting the structure of G2 antibody as well as the DNA sequences of FRs and CDRs elements of variable regions.

Suppl Figure 3: Graph depicting abundance of APOBEC 3G and 3H expression levels in Vero cells by RT-qPCR analysis. *Statistical significant: $p<0.05$.

Suppl Figure 4: APOBEC consensus RNA 2D sequence and structure motifs. **A.** Mutation profile of SARS-CoV-2 genome exhibits APOBEC mutation signatures. Applying bioinformatics analysis, C to U mutations were found to be the most dominant (55%), suggesting an APOBEC driven signature. 56.8% of these mutations were confirmed to exert APOBEC binding characteristics. **B.** Depicts the APOBEC consensus 2D structure image as obtained from Beam software with statistics for the motif as shown in **(C)** and the position of the motif on the 120 nt window as presented in **(D)**. APOBEC average probability per base of being unpaired around a 120 nt region of the most probable C→U site. **E.** The average probability from all C→U sites as obtained from the RNAplfold

algorithm is depicted (**i**) while **(ii)** presents the consensus sequence motif relative to the average probability window.

Suppl Figure 5: Infected senescent cells as a putative source for SARS-CoV-2 quasi-species generation. A. (i) Schematic layout presenting representative APOBEC sites from the GISAID database analysis that overlap with the C→ U sites of Vero cells after 17 days of infection with the SARS-CoV-2 B.1.222 strain (see also panel **B**). The yellow bars show the frequency of C→U substitutions when observing the GISAID database read counts (green pileups) and with red is the C→U frequency when observing the SARS-CoV-2 genome, 17 days post infection. These representative sites are ranked as highest relatively to the C→U counts as observed from the GISAID database. The genomic co-ordinates of each C→U can be observed at the superimposed SARS-CoV-2 genome. On the left of the graphs is the consensus motif when performing a motif analysis of all the C→U sites of the SARS-CoV-2 genome, 17 days post infection. NGS reads were confirmed in triplicate reads. **(ii)** Graph depicting frequency of nucleotide substitutions that accumulated in the genome of B.1.222 strain following 17 days of infection. **(iii)** Pie chart demonstrating that predominant C→U substitutions (65%) are APOBEC driven. **B.** Additional locations of C→U substitutions observed in the genome of the SARS-CoV-2 progeny after 17 days of infection in Vero cells (relative to panel **A**).

Material and Methods

RNA extraction and Reverse-Transcription real-time PCR (RT-qPCR) detection

SASP cytokine and APOBEC G and H mRNA analysis

RNA was extracted using the Nucleospin RNA kit (Macherey-Nagel #740955) according to the manufacturer's instructions. 1 µg RNA was used for cDNA preparation with Primescript™ RT Reagent Kit (Takara #RR037A). RT-qPCR was performed utilizing SYBR Select Master Mix (Life technologies #4472908) on a DNA-Engine-Opticon (MJ-Research) thermal cycler. Primer sequences employed were: *IL-1β* Fw: 5'-GGAAGACAAATTGCATGG-3', Rv: 5'-CCCAACTGGTACATCAGCAC-3'; *IL-6* Fw: 5'-AGAGGCACTGGCAGAAAAC-3', Rv: 5'-TGCAGGAACTGGATCAGGAC-3'; *IL-8* Fw: 5'-AGGACAAGAGCCAGGAAGAA-3', Rv: 5'-ACTGCACCTTCACACAGAGC-3'; *APOBEC3G* Fw: 5'-CCGAGGACCCGAAGGTTAC-3', Rv: 5'- TCCAACAGTGCTGAAATTCG-3'; *APOBEC3H* Fw: 5'-CGACGGCTTGAAAGGATAGAG-3', Rv: 5'- TGAGTTGTGTGTTGACGATGA-3'; B2M: β2-microglobulin (reference) gene Fw: 5'-TCTCTGGCTGGATTGGTATCT-3', Rv: 5'-CAGAATAGGCTGCTGTTCCTATC-3' (1). Results, averaged from three independent experiments, are presented as n-fold changes after Sars-CoV-2 infection relatively to the non-infected condition, using the 2-ΔΔCT method.

Viral RNA detection

RNA was extracted using the NucleoSpin Virus RNA purification kit (Macherey-Nagel #740.983) according to the manufacturer's instructions. RT-qPCR was performed utilizing the One Step PrimeScript III RT-PCR Kit (Takara # RR601B) on a Rotor-Gene Q 6000

(Qiagen) thermal cycler following the manufacturer's instructions and using the CDC N-gene directed primers [**https://www.cdc.gov/coronavirus/2019-ncov/lab/rt-pcr-panel-primer-probes.html**].

Anti-SARS-COV-2 antibodies

Generation

A series of monoclonal antibodies against SARS-CoV2 spike protein were produced according to a modified method of Koehler and Milstein (Koehler and Milstein, 1975). Briefly, twelve BALB/c mice of 5 weeks of age were immunized intraperitoneally (i.p.) with 25μg of SARS-Cov2 protein (Trenzyme GmbH, Germany). All immunization and animal handling were in accordance with animal care guidelines as specified in EU Directive 2010/63/EU. After 5 cycles of immunization, mice were sacrificed, spleenocytes were collected and fused with P3X63Ag8.653 (ATCC® CRL1580™) following a modified method of Koehler and Milstein. Positive clones and antibody specificity were determined through extensive immunosorbent assays. Four clones, namely 479-S1, 480-S2, 481-S3 and 482-S4 are under patent application (**Gorgoulis V.G., Vassilakos D. and Kastrinakis N. *(2020)* GR patent application no: 22-0003846810**).

RNA sequence determination and amino acid prediction

RNA was collected from biological duplicates of generated hybridomas as described elsewhere (2). RNA samples were processed according to manufacturer's instructions, using the following kits: NEBNext® Poly(A) mRNA Magnetic Isolation Module (E7490S), NEBNext® Multiplex Oligos for Illumina® (Index Primers Set 1, NEB7335) and

586 NEBNext® Ultra™ II Directional RNA Library Prep with Sample Purification Beads
587 (E7765S). After successful QC (RNA 6000 Nano bioanalyzer, Agilent) and quantity
588 measurements (Qubit™ RNA HS Assay Kit, Thermofisher), 1ug was used for mRNA
589 selection, cDNA construction, adaptor ligation and PCR amplification (11 cycles),
590 according to the manufacturer's protocol:
591 (https://international.neb.com/products/e7760-nebnext-ultra-ii-directional-rna-library-
592 prep-kit-for-illumina#Product%20Information). The 479-G2-ATCACG index from NEB
593 E7335 was used. The final libraries were analyzed with Agilent High Sensitivity DNA Kit on
594 an Agilent bioanalyzer, quantitated (Qubit dsDNA HS Assay Kit, Thermofisher) and, after
595 multiplexing, were run using a NextSeq 500/550 Mid Output Kit v2.5 (150 cycles), paired
596 end mode on a NextSeq550 (Illumina) at final concentration 1,3pM with 1% PhiX Control
597 v3.
598 Fastq files were demultiplexed with Flexbar (3). Quality control of the Fastq files was
599 assessed with FastQC tools (4). Adapter sequences were removed with Cutadapt program
600 (5) with the following parameters: quality trimming was set to 20 and the minimum
601 allowed nucleotide length after trimming was 20 nucleotides using --pair-filter=any to
602 apply the filters to both paired reads. A two way alignment mode was followed to
603 identify the antibody clone. More precisely alignments were performed with Bowtie2 (6)
604 with parameters set as following: -D 20 -R 3 -N 1 -L 20 -i S,1,0.50 –no-mixed --no-
605 discordant against an index made from IMGT database http://www.imgt.org/ having
606 downloaded all mouse and human IG genes. Also this mode of alignments was executed
607 for quality control and visualization of the aligned reads spanning the IG gene segments
608 on the genome browser. The second mode refers to the determination and

609 reconstruction of the clones. This was performed with MiXCR suite (7). At first,
610 alignments against the IG repertoire were performed with kaligner and visualization of
611 alignments was assessed. It was observed that the use of kaligner gave better results
612 with higher clone hits regarding the VH and VL segments. Full assembly of the clones was
613 performed. A full report of the number of reads and assembly of CDR and FR clones is
614 provided in clones479_S1kalign.txt. The clones with the highest number of reads and
615 coverage across the V,D,J segments were considered. The reported matched sequences
616 were also checked with IgBlast tool https://www.ncbi.nlm.nih.gov/igblast/. In addition,
617 after the assembly of the amino acid reconstruction of the FR and CDR regions of the full
618 variable fragment for both the Heavy and Light antibody chains, a 3D visualization was
619 also determined via folding the V protein fragment with iTassser suite (8). The above
620 analysis has been extensively described in **Gorgoulis VG, Vassilakos D and Kastrinakis N.**
621 ***(2020)* GR patent application no: 22-0003846810**.
622
623 **Immunocytochemistry (ICC)-Immunohistochemistry (IHC)**
624 Method: ICC and IHC were performed according to previous published protocols (9). In
625 brief, 3 μm thick sections from formalin-fixed paraffin embedded (FFPE) lung tissues were
626 employed. Antigen retrieval was heat-mediated in 10 mM citric acid (pH 6.0) for 15
627 minutes. The following primary antibodies were applied: i) the anti-SARS-CoV-2 (G2)
628 monoclonal antibody (dilution 1:300), ii) anti-ACE-2 [Rabbit polyclonal antibody Abcam,
629 Cat.no: ab15348 (dilution 1:200)], iii) anti- TTF-1 [rat monoclonal antibody Dako, Clone
630 8G7G3/1, Cat.no: M3575 (Ready-to-Use)], iv) anti-CD68 [mouse monoclonal antibody
631 Dako, Clone PG-M1, Cat.no: M0876 (dilution 1:50)] and v) anti-$p16^{INK4A}$ [mouse

monoclonal antibody Santa Cruz, clone: F-12, Cat.no.:sc-1661. (dilution 1:100)], vi) IL-1β [Rabbit polyclonal antibody Abcam, Cat.no: ab2105 (dilution 1:150)] and vii) IL-6 [mouse monoclonal antibody R&D systems, clone: Clone: 6708, Cat.no:MAB206 (dilution 1:100)], all overnight at 4°C. Development of the signal was achieved using the Novolink Polymer Detection System (Cat.no: RE7150-K, Leica Biosystems). Specimens were counterstained with hematoxylin.

Negative Controls for the anti-SARS-CoV-2 (G2) monoclonal antibody: *i) Biological,* comprising previously published and new lung tissue samples from a cohort of 50 cases that underwent surgery prior to COVID-19 outbreak. *ii) Technical:* a. Omission of the G2 primary monoclonal antibody, b. Blocking of the G2 primary monoclonal antibody using the corresponding S-protein (Cat.no.P2020-029, Trenzyme) in a 1:10 (G2/Spike protein) ratio and c. Two slides per case were employed for each staining or control experiment.

Evaluation of G2 staining: Cells were considered positive irrespective of the staining intensity. Two different semi-quantitative IHC evaluation approaches, previously described were adopted (10,11) According to the first, the number of G2 positive cells per 4mm^2 was encountered and scored according to the following criteria: (+) for positive staining in<5 cells per 4 mm^2, (+) for positive staining in 5–50 cells per 4mm^2 and (+++) for positive staining in >50 cells per 4 mm^2 (10). Regarding the second one, the number of G2 positive cells per whole slide was estimated and subsequent scores were assessed: (+) between one and five positive cells per whole slide (scattered cells), (++) more than five cells per whole slide but no foci (isolated cells) and (+++) more than 10 cells in one × 20 field (with foci) (11). For IL-6 and IL-1b, the percentage of immunopositive cells was

654 encountered (12). Evaluations were performed blindly by four experienced pathologists
655 (KE, PF, CK and VG) and intra-observer variability was minimal ($p \leq 0.05$).
656
657 **Bioinformatic analysis for identification of mutational signatures in the SARS-CoV-2**
658 **genome**
659 ***Screening for mutational signatures in the SARS-CoV-2 genome***
660 To investigate the mutational properties on the SARS-CoV-2 genome we downloaded from
661 GISAID database (**https://www.gisaid.org/**) 423.000 available strains that were
662 distributed globally. These strains were aligned with the Wuhan first assembly
663 NC_045512, obtained from NCBI (**https://www.ncbi.nlm.nih.gov/sars-cov-2/**), with
664 Bowtie aligner (13) using the following command:
665 /bowtie2-2.4.2-sra-linux-x86_64/bowtie2-align-s --wrapper basic-0 -x Covncbiref -p 4 -D
666 20 -R 3 - N 1 -L 20 -i S,1,0.50 -f allCov19.fa
667 In order to identify the mutations we have created an "in-house" script using *calmd*
668 function from SAMtools (14) , based on the analysis of deciphering mutations from the
669 proteome occupancy profile study (15). We applied the following commands for minus
670 and reverse stranded reads:
671 *samtools sort accepted_hits.bam -o accepted_hitsort.bam*
672 *samtools rmdup -s accepted_hitsort.bam rmdupsorted.bam*
673 *#forward library*
674 *samtools view -h -f 0x0010 rmdupsorted.bam | samtools calmd -S -*
675 *~/Desktop/Bioinformatics/NCBI.fa /dev/stdin |*

/media/covid_meth/deademination_covid19/get_edit_stat.pl '-' > Mapping_editStatus.bed

samtools view -h -F 0x0010 rmdupsorted.bam | samtools calmd -S - ~/Desktop/Bioinformatics/NCBI.fa /dev/stdin | /media/covid_meth/deademination_covid19/get_edit_stat.pl '+' >> Mapping_editStatus.bed

#reverse library

samtools view -h -F 0x0010 rmdupsorted.bam | samtools calmd -S - ~/Desktop/Bioinformatics/GRCh37/hg19.fa /dev/stdin | /media//covid_meth/deademination_covid19/get_edit_stat.pl '-' > Mapping_editStatus2.bed

samtools view -h -f 0x0010 rmdupsorted.bam | samtools calmd -S - ~/Desktop/Bioinformatics/GRCh37/hg19.fa /dev/stdin | /media//covid_meth/deademination_covid19/get_edit_stat.pl '+' >> Mapping_editStatus2.bed

The scripts bellow were used in order to determine the counts per type of mutation and filter for C→U or G→A mutations in respect with the strand orientation of the alignments. Bedtools (16) have also been used to obtain the fasta sequences and the windows around the C→U sites.

#sort reads

sort -k1,1 -k2,2n -k3,3n*Mapping_editStatus2.bed* | uniq -c > Mapp_editstat_APOBECcounts.bed sort -k1,1 -k2,2n -k3,3n*Mapping_editStatus2.bed* |

uniq -c > Mapp_editstat_APOBECcounts.bed sed -i 's/^ *//g' Mapp_editstat_APOBECcounts.bed

#obtain the fasta

fastaFromBed -s -fi ~/Desktop/Bioinformatics/GRCh37/hg19.fa -bedMapp_editstat_APOBECcounts.bed -tab -foAPOBEC_counts1fa.bed

#get mutation type C→ U or A→G

perl fixmutstat.pl APOBEC_counts1fa.bed APOBEC_counts1facorrect

Based on the filtered candidate sites with a frequency of mutations above than 5 reads we have obtained windows of ±60 nucleotides and folded the RNA sequences from these regions with Vienna RNA fold algorithm (17) to determine the RNA 2D structure. SHAPE reactivities from SHAPE-seq data (18) were used to guide the RNA folding.

RNAfold --noPS --shape=forViennatest.SHAPE.txt –shapeConversion=S -g < forViennatest..fa >> test.txt.

To decipher the candidate motifs we counted the frequency of letters ±5 nucluteotides from the most frequent deademinated nucleotide. The frequency for each letter was determined via a perl script which extracts all possible *k-mers* and their frequencies. Next these *k-mers*, based on their frequency, were plotted with Web-logo motifs (19). In addition position-weight matrices (PWM) for each letter around the deadiminated RNA nucleotide were extracted.

Our analysis on motifs and RNA structure for choosing the candidate APOBEC sites based on publicly available known studies (20-22) that also demonstrate similar characteristics regarding the motif specific APOBEC signature and RNA structure. From our analysis we

721 determined a CCT/A enrichment around regions of open hairpin structures agreeing with
722 the results from the literature.
723
724 ***Verification of APOBEC specific motifs by applying machine learning***
725 To filter and obtain scores for each APOBEC specific candidate site we have also applied a
726 machine learning scheme using convolutional neural networks having as input the
727 sequence and RNA structure around the candidate strongest APOBEC sites with high
728 frequency that also demonstrate a high potential for APOBEC binding.
729
730 ***APOBEC consensus RNA 2D sequence and structure motifs***
731 To determine the consensus RNA structure properties we have used the Vienna RNA
732 folding output dot bracket notation, which performed the folding based on the icSHAPE
733 reactivities as input to BEAM program (23). In addition, the binding sites from (19) have
734 been used to decipher the structure for the hg19. The structure properties for the
735 APOBEC sites on the hg19 have been folded using SHAPE (24) and DMS (25) data to guide
736 the RNA folding. Secondary RNA structure motifs regarding the hg19 have been
737 determined using BEAM software. Beam software was used as follows:
738 First the dot bracket notation is translated in a 24 letter language for structure called
739 Bear:
740 *java -jar encoder.jar APOBEC.db APOBEC.fb*
741 *java -jar /$basepath3/BEAM_release_1.5.1.jar -f APOBEC.fb -w 15 -W 30 -M 5*
742 Next, then consensus motifs are extracted, using as maximum threshold to output the
743 top 5 motifs with maximum width of motif set to 30 nucleotides.

APOBEC average probability per base of being unpaired around a 120 nt region of the most probable C→U site

Furthermore RNAplfold has been used to extract the probabilities per base of being unpaired having the following parameters

RNAplfold -W 30 -L 15 -u 1 --shape=forViennatest.SHAPE.txt --shapeMethod=D --shapeConversion=O -g < forViennatest..fa >> test.txt

The output per sequence is a *_lunp* file where from these files the smoothed geometric mean per base pair is extracted and plotted having the candidate deaminated site, located in the center of the 120 nucleotide window. The plots are done in R using fit and polygon functions from the standard R bioconductor packages. The confidence intervals per base are calculated as CI=$\bar{x} \pm z\frac{s}{\sqrt{n}}$where z =0.95 % confidence, *s*=standard deviation and *n* are the number of sequences ~3500.

In order to accomplish docking of the APOBEC with the RNA substrates we have used SimRNA suite (26) to determine the RNA 3D structure properties of the SARS-CoV-2 RNA around the candidate C→U sites. DARS-RNP potential (27) has been used using PDB files from crystallographic data for APOBEC3G with PDB code 6bux and 6k3j (28) from the PDB database (**https://www.rcsb.org/)** for docking the RNAs as obtained from SimRNA with APOBEC. Scores were ranked and the RNAs with docking scores higher than 1 standard deviation over the mean were used for the extraction of consensus motifs both in terms of structure and sequence. Regarding the sequence motif a window of ±10 nt around the high docking score was obtained and according to the *k-mer* distribution PWM matrices are extracted and plotted with web-logo.

The SimRNA commands to extract the 3D RNA structure are the following:

./SimRNA -s 3D_testVf.fa -c config2.dat -S 3D_test.struct -o tRNAs python2 trafl_extract_lowestE_frame.py tRNAs.trafl"

./SimRNA_trafl2pdbs tRNAs-000001.pdb tRNAs_minE.trafl : AA" perl configpdb2.pl tRNAs_minE-000001_AA.pdb tRNAs.config"

The configuration file for the 3D simulations is set as:

NUMBER_OF_ITERATIONS 160000

TRA_WRITE_IN_EVERY_N_ITERATIONS 16000

INIT_TEMP 1.35

FINAL_TEMP 0.90

BONDS_WEIGHT 1.0

ANGLES_WEIGHT 1.0

TORS_ANGLES_WEIGHT 0.0

ETA_THETA_WEIGHT 0.40

SECOND_STRC_RESTRAINTS_WEIGHT 1.0

FRACTION_OF_NITROGEN_ATOM_MOVES 0.10

FRACTION_OF_ONE_ATOM_MOVES 0.45

FRACTION_OF_TWO_ATOMS_MOVES 0.44

FRACTION_OF_FRAGMENT_MOVES 0.01

In order to visualize the properties that might determine the binding of APOBEC, the power of integrated gradients tools (29) were used to obtain the motifs. Our analysis is based upon an already developed method DeepRipe (30) adding an extra module to also

789 incorporate the RNA structure information. The classifier has been trained to distinguish

790 such motifs which are characteristic for APOBEC binding.

791

Supplementary References

1. Huan CC, Wang HX, Sheng XX, Wang R, Wang X, Liao Y, Liu QF, Tong GZ, Ding C, Fan HJ, Wu JQ, Mao X. Porcine epidemic diarrhea virus nucleoprotein contributes to HMGB1 transcription and release by interacting with C/EBP-β. Oncotarget 2016; 7; 75064–75080.

2. Komseli ES, Pateras IS, Krejsgaard T, Stawiski K, Rizou SV, Polyzos A, Roumelioti FM, Chiourea M, Mourkioti I, Paparouna E, Zampetidi s CP, Gumeni S, Trougakos IP, Pefani DE, O'Neill E, Gagos S, Eliopoulos AG, Fendler W, Chowdhury D, Bartek J, Gorgoulis VG. A prototypical non-malignant epithelial model to study genome dynamics and concurrently monitor micro-RNAs and proteins in situ during oncogene-induced senescence. BMC Genomics 2018; 19: 37.

3. Dodt M, Roehr JT, Ahmed R, Dieterich C. FLEXBAR-Flexible Barcode and Adapter Processing for Next-Generation Sequencing Platforms. Biology (Basel) 2012; 1: 895–905.

4. Andrew SA. quality control tool for high throughput sequence data. Fast QC 2010; 532.

5. Martin M. Cutadapt removes adapter sequences from high-throughput sequencing reads. EMBnet J 2011: 17: 10-12.

6. Langmead B, Salzberg SL. Fast gapped-read alignment with Bowtie 2. Nat Methods 2012; 9: 357-359.

7. Bolotin DA, Poslavsky S, Davydov AN, Frenkel FE, Fanchi L, Zolotareva OI, Hemmers S, Putintseva EV, Obraztsova AS, Shugay M, Ataullakhanov RI, Rudensky AY, Schumacher TN, Chudakov DM. Antigen receptor repertoire profiling from RNA-seq data. Nat Biotechnol 2017; 35: 908–911.

814 8. Yang J, Yan R, Roy A, Xu D, Poisson J, Zhang Y. The I-TASSER Suite: protein structure
815 and function prediction. Nature Methods 2015; 12: 7–8.
816 9. Evangelou K, Lougiakis N, Rizou SV, Kotsinas A, Kletsas D, Muñoz-Espín D,
817 Kastrinakis NG, Pouli N, Marakos P, Townsend P, Serrano M, Bartek J, Gorgoulis VG.
818 Robust, universal biomarker assay to detect senescent cells in biological specimens.
819 Aging Cell 2017; 16: 192–197.
820 10. Schaefer IM, Padera RF, Solomon IH, Kanjilal S, Hammer MM, Hornick JL, Sholl LM.
821 In situ detection of SARS-CoV-2 in lungs and airways of patients with COVID-19. Mod
822 Pathol 2020; 33: 2104–2114.
823 11. Remmelink M, De Mendonça R, D'Haene N, De Clercq S, Verocq C, Lebrun L, Lavis P,
824 Racu ML, Trépant AL, Maris C, Rorive S, Goffard JC, De Witte O, Peluso L, Vincent JL,
825 Decaestecker C, Taccone FS, Salmon I. Unspecific post-mortem findings despite
826 multiorgan viral spread in COVID-19 patients. Crit Care 2020; 24: 495.
827 12. van Vliet T, Varela-Eirin M, Wang B, Borghesan M, Brandenburg SM, Franzin R,
828 Evangelou K, Seelen M, Gorgoulis V, Demaria M. Physiological hypoxia restrains the
829 senescence-associated secretory phenotype via AMPK-mediated mTOR suppression. Mol
830 Cell 2021; S1097-2765(21)00213-6.
831 13. Langmead B, Trapnell C, Pop M, Salzberg SL. Ultrafast and memory-efficient
832 alignment of short DNA sequences to the human genome. Genome Biol 2009; 10: R25.
833 14. Li H, Handsaker B, Wysoker A, Fennell T, Ruan J, Homer N, Marth G, Abecasis G,
834 Durbin R; 1000 Genome Project Data Processing Subgroup. The Sequence
835 Alignment/Map format and SAMtools. Bioinformatics 2009; 25: 2078–2079.

836 15. Schueler M, Munschauer M, Gregersen LH, Finzel A, Loewer A, Chen W, Landthaler
837 M, Dieterich C. Differential protein occupancy profiling of the mRNA transcriptome.
838 Genome Biol 2014; 15: R15.
839 16. Quinlan AR, Hall IM. BEDTools: a flexible suite of utilities for comparing genomic
840 features. Bioinformatics 2010; 26: 841–842.
841 17. Gruber AR, Lorenz R, Bernhart SH, Neuböck R, Hofacker IL. The Vienna RNA
842 websuite. Nucleic Acids Res 2008; 36(Web Server issue): W70–W74.
843 18. Manfredonia I, Nithin C, Ponce-Salvatierra A, Ghosh P, Wirecki TK, Marinus T,
844 Ogando NS, Snijder EJ, van Hemert MJ, Bujnicki JM, Incarnato D. Genome-wide mapping
845 of SARS-CoV-2 RNA structures identifies therapeutically-relevant elements. Nucleic Acids
846 Res 2020; 48: 12436–12452.
847 19. Crooks GE, Hon G, Chandonia JM, Brenner SE. WebLogo: a sequence logo
848 generator. Genome Res 2004; 14: 1188–1190.
849 20. Sharma S, Patnaik SK, Taggart RT, Baysal BE. The double-domain cytidine
850 deaminase APOBEC3G is a cellular site-specific RNA editing enzyme. Sci Rep 2016; 6:
851 39100.
852 21. Sharma S, Baysal BE. Stem-loop structure preference for site-specific RNA editing
853 by APOBEC3A and APOBEC3G. PeerJ 2017; 5: e4136.
854 22. York A, Kutluay SB, Errando M, Bieniasz PD. The RNA Binding Specificity of Human
855 APOBEC3 Proteins Resembles That of HIV-1 Nucleocapsid. PLoS Pathog 2016; 12:
856 e1005833.

857 23. Pietrosanto M, Mattei E, Helmer-Citterich M, Ferrè F. A novel method for the
858 identification of conserved structural patterns in RNA: From small scale to high-
859 throughput applications. Nucleic Acids Res 2016; 44: 8600–8609.
860 24. Spitale RC, Flynn RA, Zhang QC, Crisalli P, Lee B, Jung JW, Kuchelmeister HY, Batista
861 PJ, Torre EA, Kool ET, Chang HY. Erratum: Structural imprints in vivo decode RNA
862 regulatory mechanisms. Nature 2015; 527: 264.
863 25. Rouskin S, Zubradt M, Washietl S, Kellis M, Weissman JS. Genome-wide probing of
864 RNA structure reveals active unfolding of mRNA structures in vivo. Nature 2014; 505:
865 701–705.
866 26. Boniecki MJ, Lach G, Dawson WK, Tomala K, Lukasz P, Soltysinski T, Rother KM,
867 Bujnicki JM. SimRNA: a coarse-grained method for RNA folding simulations and 3D
868 structure prediction. Nucleic Acids Res 2016; 44: e63.
869 27. Tuszynska I, Bujnicki JM. DARS-RNP and QUASI-RNP: new statistical potentials for
870 protein-RNA docking. BMC Bioinformatics 2011; 12: 348.
871 28. Maiti A, Myint W, Kanai T, Delviks-Frankenberry K, Sierra Rodriguez C, Pathak VK,
872 Schiffer CA, Matsuo H. Crystal structure of the catalytic domain of HIV-1 restriction factor
873 APOBEC3G in complex with ssDNA. Nat Commun 2018; 9: 2460.
874 29. Sundararajan, Mukund, Ankur Taly, and Qiqi Yan. "Axiomatic attribution for deep
875 networks." In International Conference on Machine Learning, pp. 3319-3328. PMLR,
876 2017.
877 30. Ghanbari M, Ohler U. Deep neural networks for interpreting RNA-binding protein
878 target preferences. Genome Res 2020; 30: 214–226.

FIGURE 1

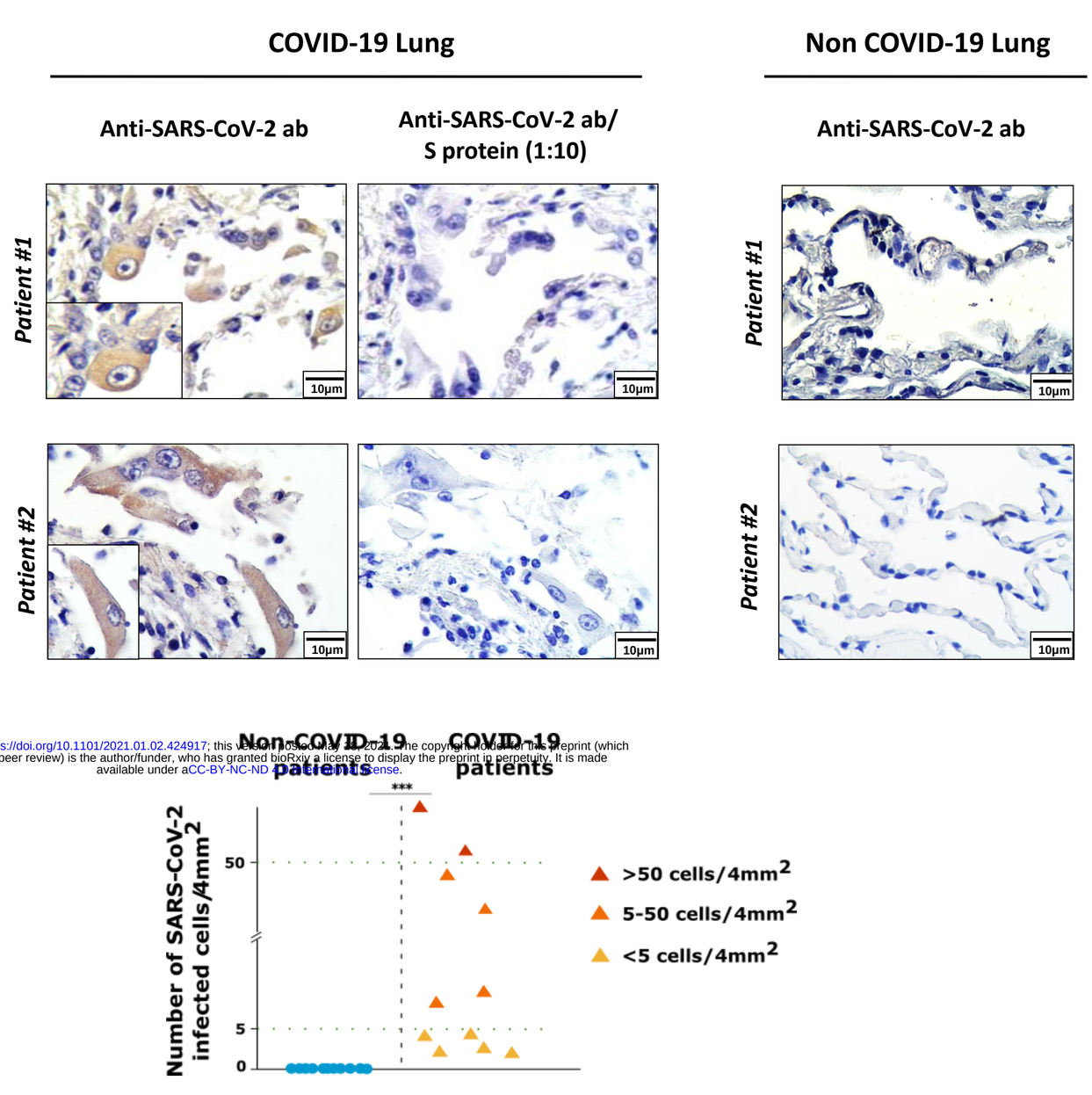

FIGURE 2.

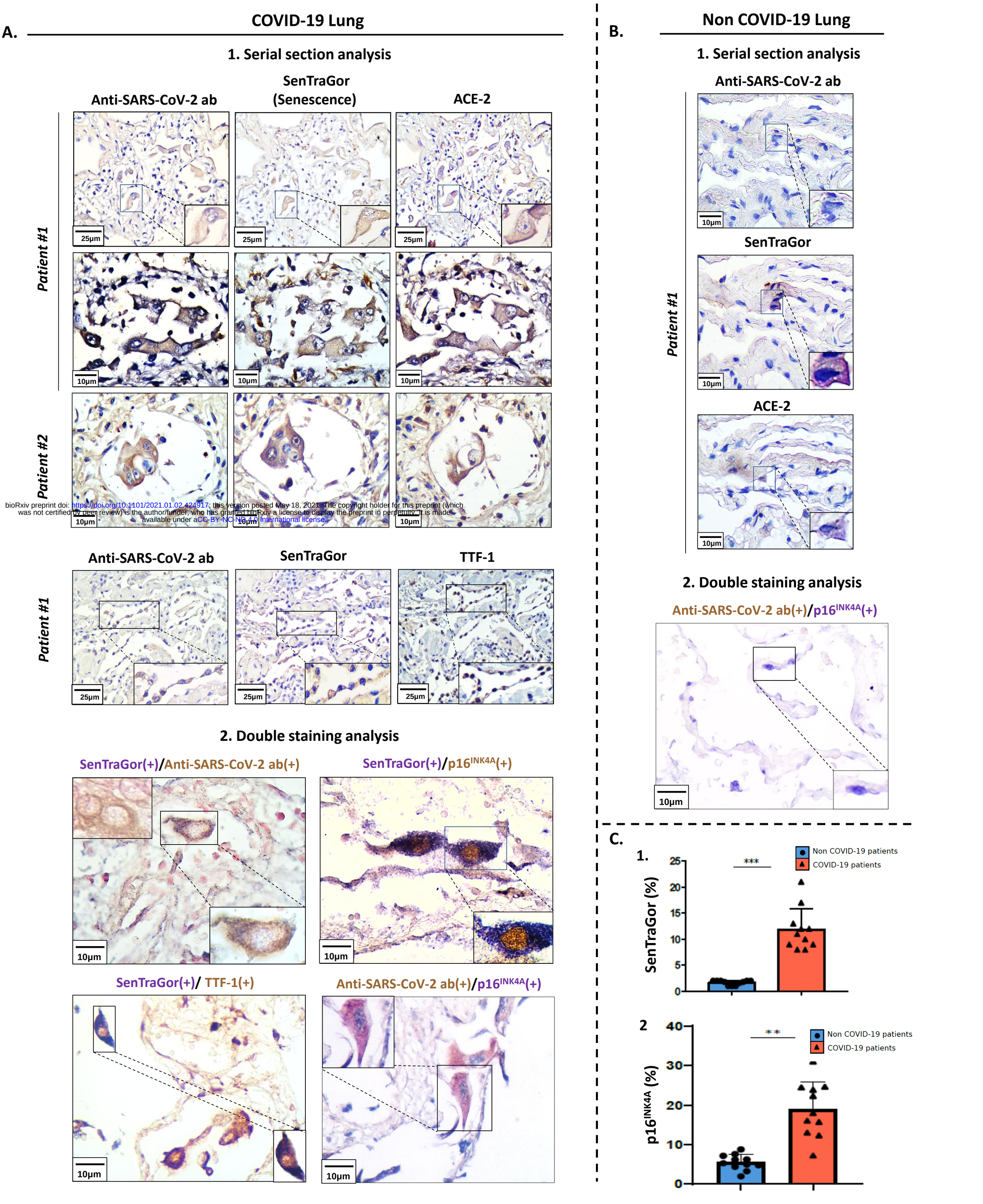

Figure 3

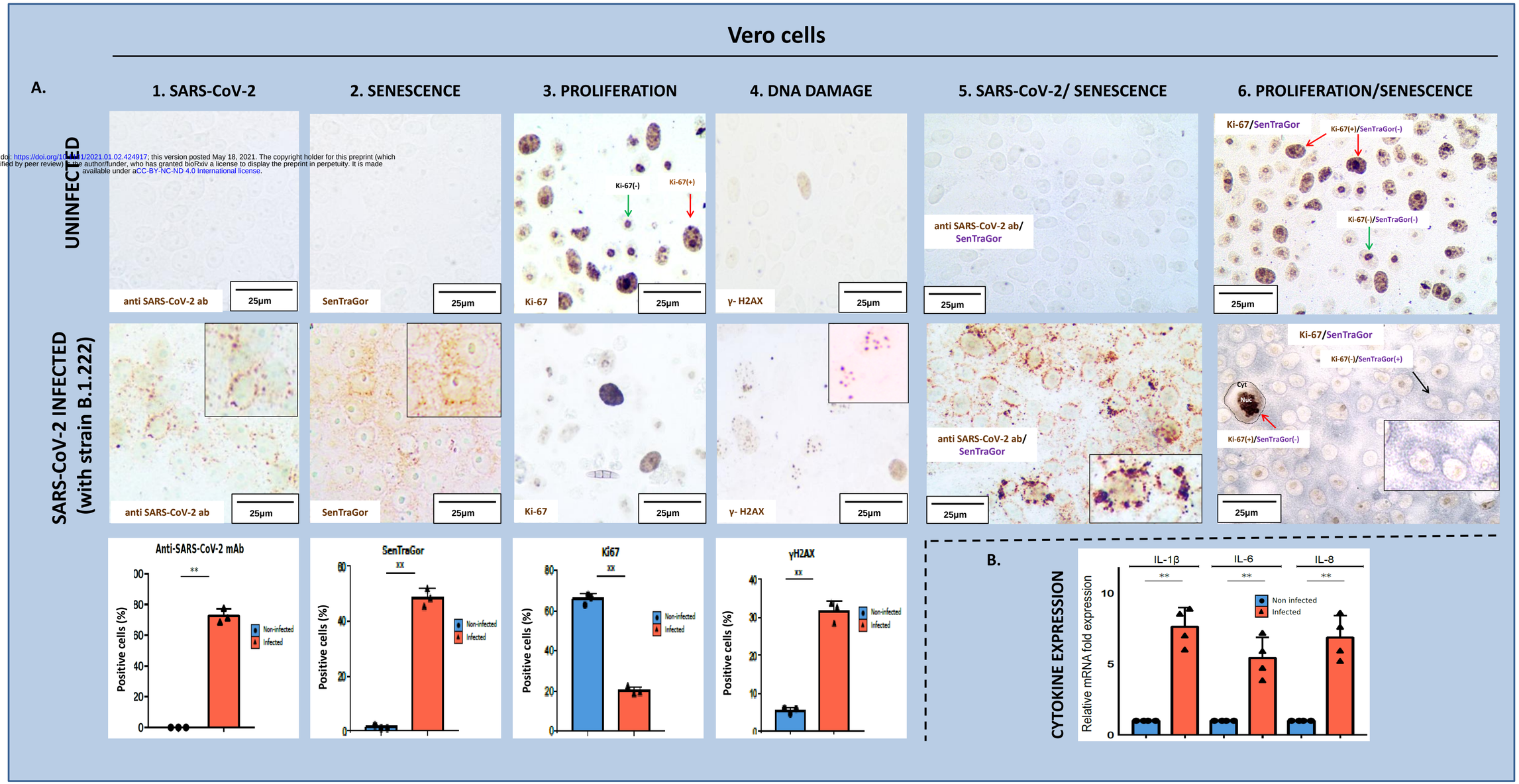

FIGURE 4.